Supplementary Information

Reconstruction of Photovoltaic Waste Silicon into Amorphous Silicon Nanowire Anodes

Liao Shen,‡[a] Kaiwen Sun,‡[c] Fengshuo Xi,‡[a] Zhitao Jiang,[a] Shaoyuan Li,*[a] Yanfeng Wang,[a] Zhongqiu Tong,[a] Jijun Lu,*[a] Wenhui Ma,*[ab] Martin Green,[c] and Xiaojing Hao*[c]

[a] Faculty of Metallurgical and Energy Engineering, Key Laboratory of Complex Nonferrous Metal Resources Clean Utilization, Kunming University of Science and Technology, Kunming 650093, China

[b] School of Engineering, Yunnan University, Kunming 650500, China

[c] Australian Centre for Advanced Photovoltaics, School of Photovoltaic and Renewable Energy Engineering, University of New South Wales, Sydney, NSW, 2052 Australia

*Corresponding author. E-mail: lsysilicon@kust.edu.cn; jjlu@kust.edu.cn; mawenhui@ynu.edu.cn; xj.hao@unsw.edu.au

Table S1 The impurity content in wSi powder was detected by ICP-AES.

Impurity content of wSi powder							
Elements	Fe	Cu	Ni	Al	Co	Zn	Cr
(ppmw)	91.41	34.22	76.68	43.05	<0.80	2.60	1.30

The impurity composition and content of the wSi were detected using an inductively coupled plasma atomic emission spectrometer (ICP-AES), with results as shown in Table S1. These results show that the main impurities are Fe, Cu, Ni, and Al, which are mainly introduced externally from the Si wafer cutting process. It can meet the Si purity requirements for use in LIB anodes.

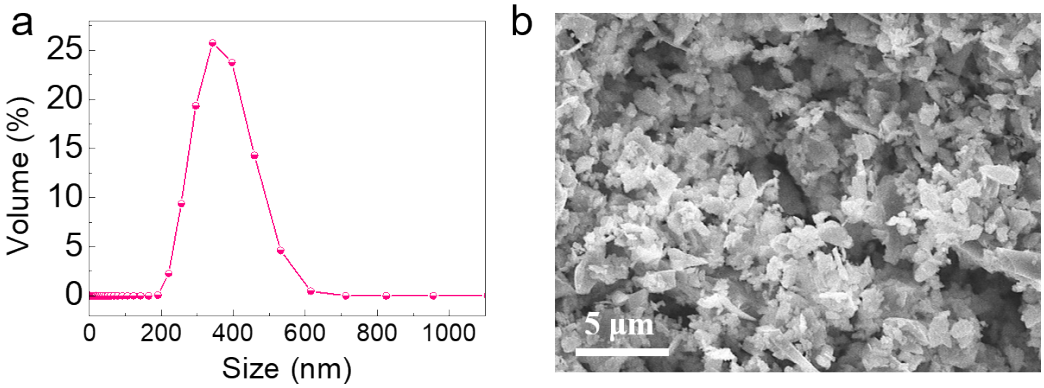

Fig. S1 (a) Particle size distribution and (b) SEM of wSi.

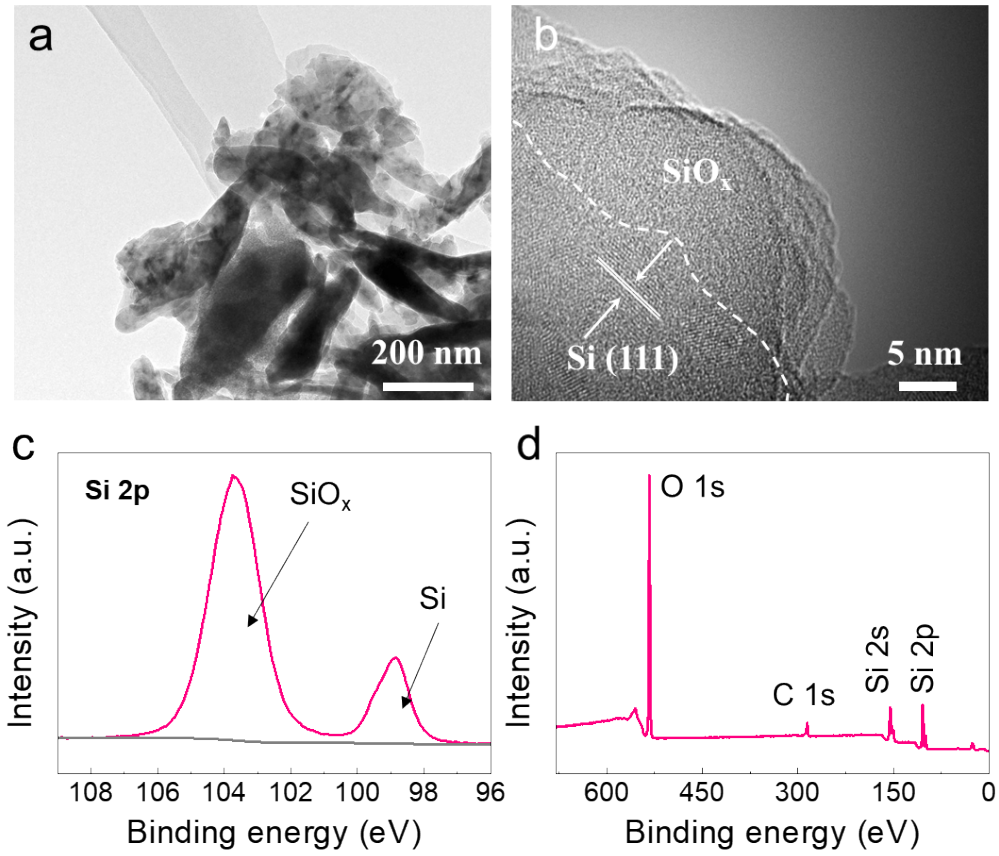

Fig. S2 (a) TEM, (b) HRTEM, (c) Si 2p, and (d) full spectrum of XPS spectra wSi. In addition,Oxygen content was measured at 5.3% using an oxygen-nitrogen-hydrogen analyzer.

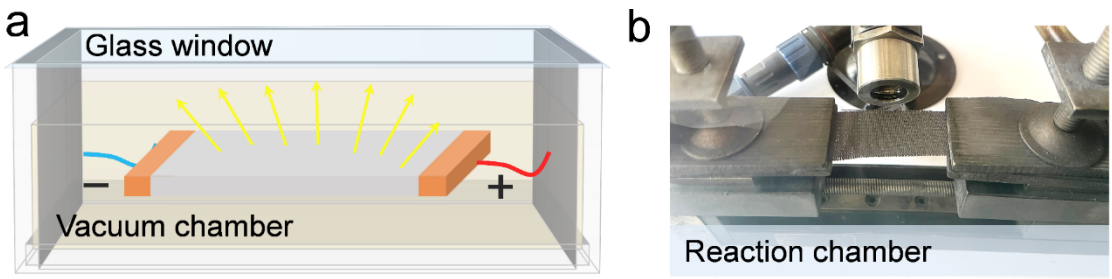

Fig. S3 (a) Schematic diagram of the CTS reaction chamber; (b) Corresponding equipment photo.

Table S2 Carbon cloth product specifications

Item	Type	Specification	Unit
Thickness	Using TECLOCK SM-11	0.36 ± 0.03	mm
Nominal Basis Weight	ASTM D-646	135 ± 20	g m^{-2}
Air Permeability	Gurley Method	< 10	second
Resistance (Through Plate)	Base on ASTM C-611	< 5	mΩ cm^2

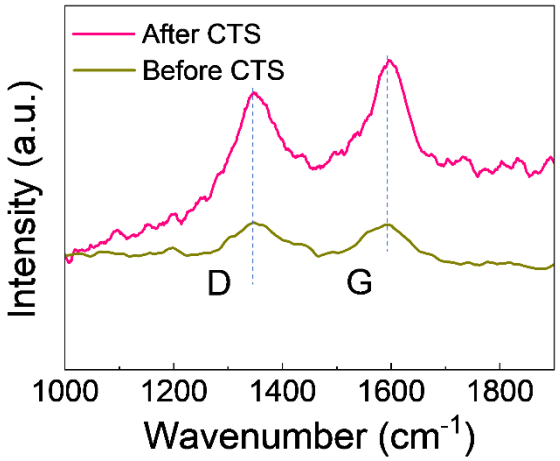

Fig. S4 Raman spectra of carbon cloth. The Raman spectrum shows that the carbon substrate exhibits weak defect (D) and graphitization (G) peaks, which are consistent with the results observed in wSi@CC. Notably, after high-temperature thermal shock, the intensity of both the D and G peaks increases, indicating the introduction of more defects, which facilitates the deposition and nucleation of Si nanowires. In summary, the carbon substrate plays a crucial role in the growth of Si nanowires in the following aspects: (i) Thermal conductivity, the high thermal conductivity of the carbon substrate helps establish a steep temperature gradient, promoting the directional diffusion and nucleation of Si atoms. (ii) Physical structure, the fibrous structure of the carbon cloth provides a large surface area, facilitating uniform growth of Si nanowires. (iii) Interfacial effects, the defect sites on the carbon surface promote Si deposition and nucleation, influencing the morphology and orientation of the nanowires.

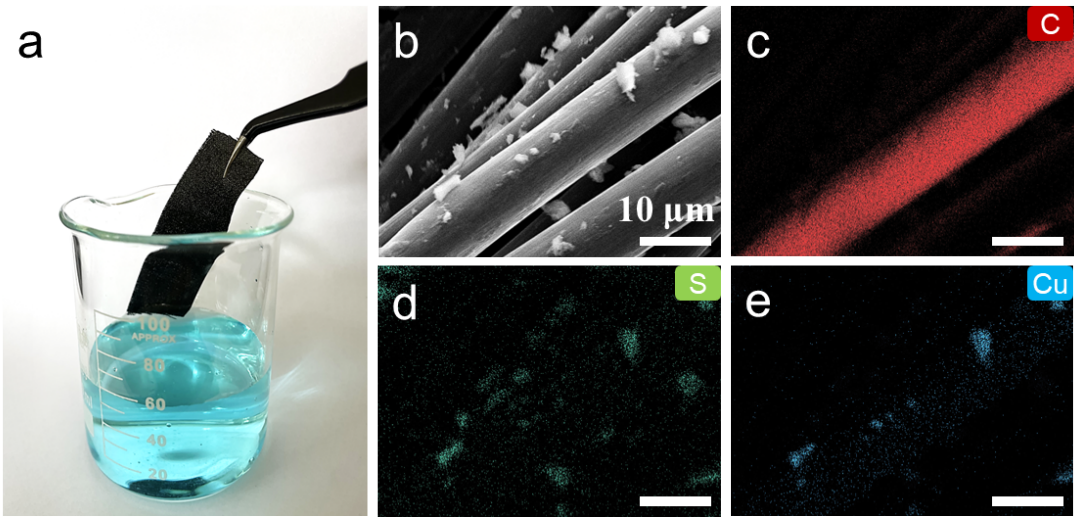

Fig. S5 (a) Carbon cloth soaked in copper sulfate solution; (b-e) SEM and element mapping before CTS of Cu sulfate attached to carbon cloth. Clearly, from the above image, the distribution of Cu and S elements is observed but appears relatively sparse. This is attributed to the insufficient adhesion of Cu salts before CTS, resulting in significant detachment during sample preparation.

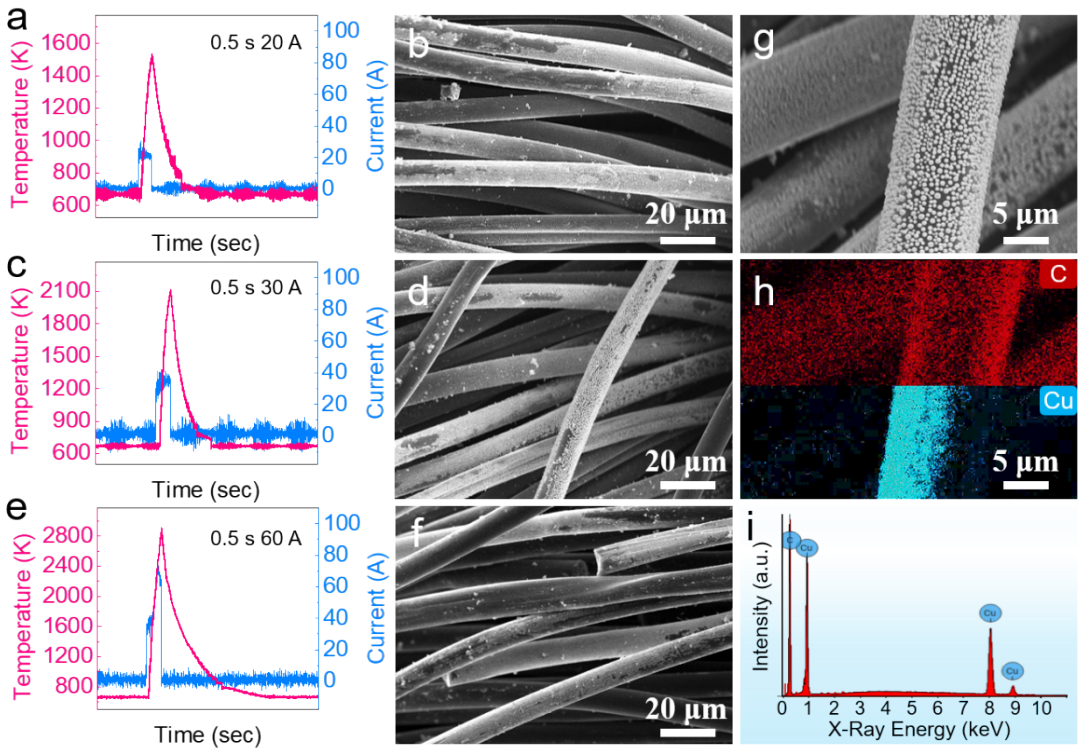

Fig. S6 (a) Morphology after CTS of copper salts at (a, b) 0.5 s, 20A, (c, d) 0.5 s, 30 A and (e, f) 0.5 s, 60 A and (g-i) the distribution of Cu and C elements after CTS at 0.5 s 30A. Based on related reports, experiments were conducted with a reaction time of 0.5 s. From Fig. S6a-i, it can be seen that the distribution of Cu particles is relatively uniform, and there is a slight decrease as the temperature increases, possibly due to local high-temperature volatilization.

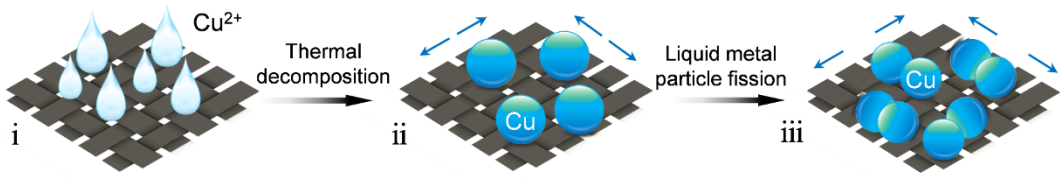

Fig. S7 Schematic diagram of the process of obtaining Cu nanoparticles from copper salts via CTS. As the temperature increases rapidly, the metal salts undergo instant pyrolysis.

$$CuSO_4 \xrightarrow{\triangle} Cu(l) + SO_x\uparrow \ (1 \le x \le 4)$$

The formed metal Cu nanoparticles will be in liquid phase and can move freely on the surface of carbon cloth. Driven by high temperature, the liquid metal Cu droplets will move quickly on the carbon cloth surface and split ("fission"). Eventually attaching to the carbon cloth substrate.[1-3]

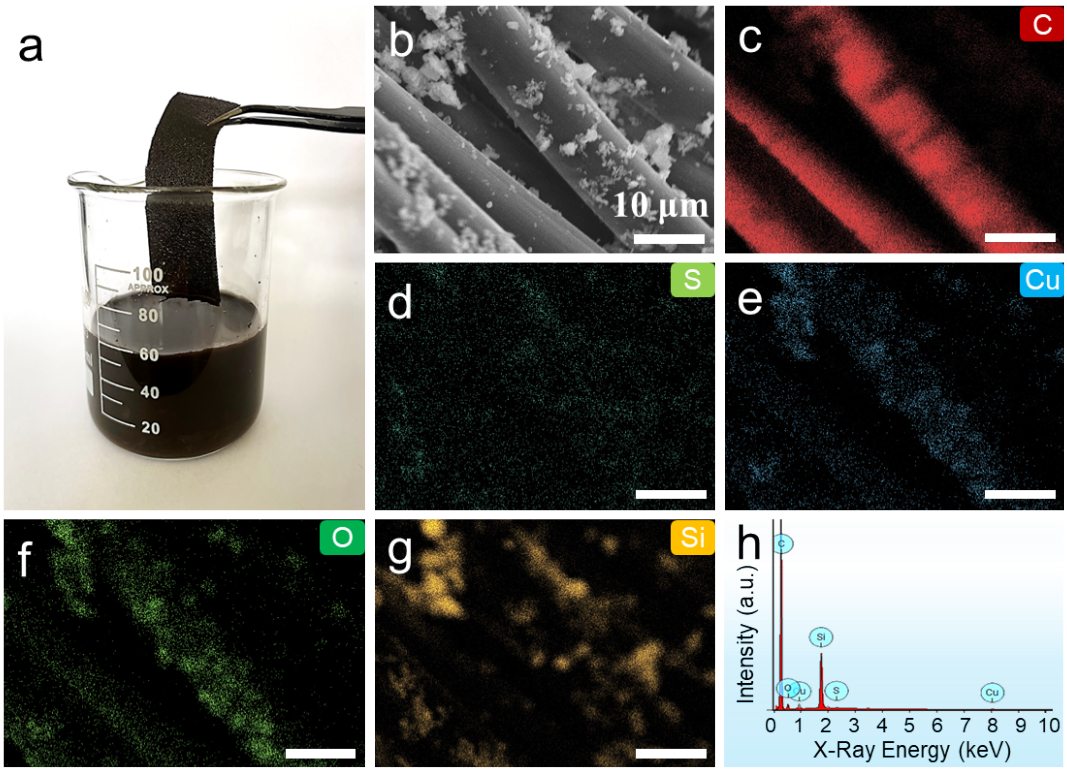

Fig. S8 (a) Carbon cloth soaked in a uniform slurry of copper sulfate and wSi, (b-h) SEM and elemental mapping of the carbon cloth with attached Cu sulfate and wSi before CTS.

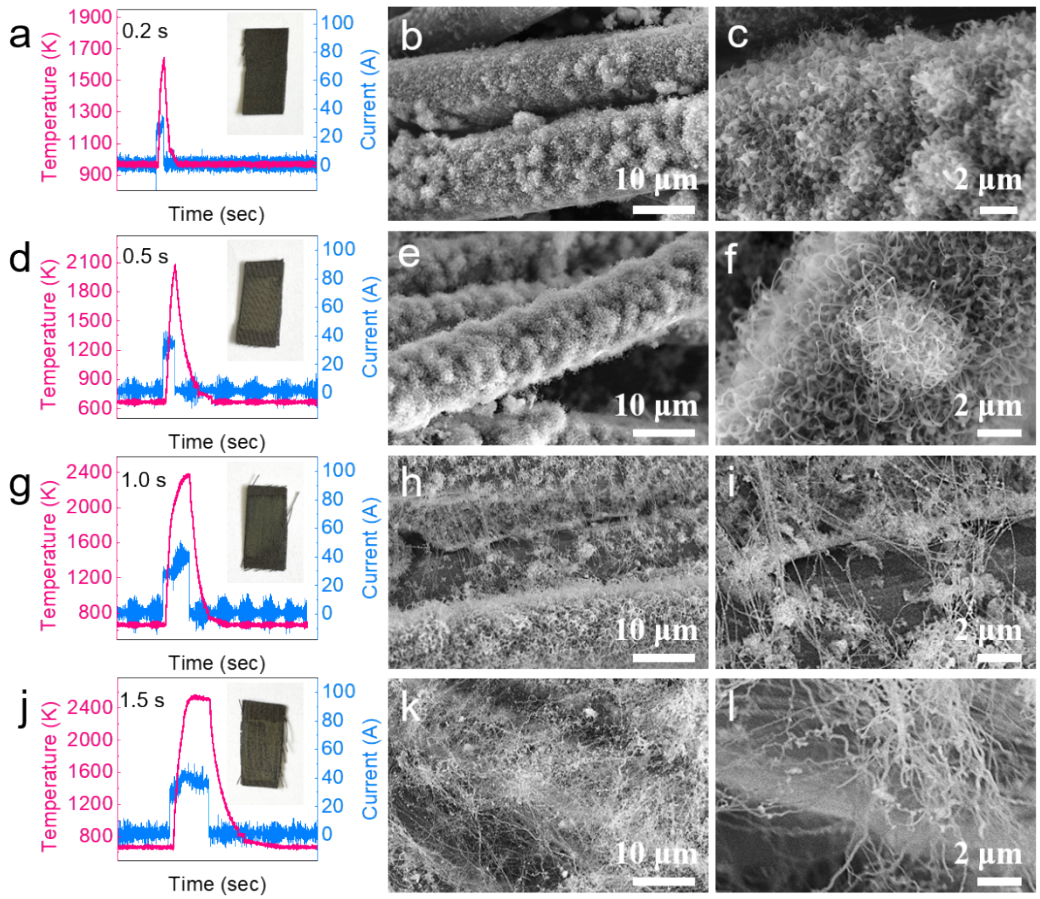

Fig. S9 Various times were set to explore the growth morphology of a-SiNWs@CC. Set the voltage and current to 30 V and 30 A, respectively, to conduct CTS experiments on the carbon cloth soaked in Cu sulfate and wSi. (a-c) correspond to temperature and current changes as well as different magnifications of morphology at 0.2 s, (d-f) correspond to 0.5 s, (g-i) correspond to 1.0 s, and (j-l) correspond to 1.5 s. It can be observed that at a shorter time (0.2 s), the growth of Si nanowires is not very evident, appearing short and aggregated. At 0.5 s, they are clearly visible and uniform. As the time increases, the temperature also rises, leading to the growth of long and disordered Si nanowires (Fig. S9g-l). According to previous research, when Si nanowires are long and disordered, they easily lose electrical contact with the current collector carbon cloth, leading to failure. Therefore, the optimized experimental conditions (30 V, 30 A, 0.5 s) were selected for further study. The insets in the temperature graphs correspond to the optical images of Si nanowires growth on the carbon cloth obtained after the respective reaction times.

Table S3 Parameters and temperature variations in CTS experiments.

Sample loaded on carbon cloth	Copper salt			Copper salt and wSi			
Voltage (V)	30	30	30	30	30	30	30
Current (A)	20	30	60	30	30	30	30
Resistance (Ω)	1.98	2.01	2.05	2.03	2.02	2.05	2.00
Time (sec)	0.5	0.5	0.5	0.2	0.5	1.0	1.5
Temperature (K)	1520	2098	2891	1655	2100	2368	2481
Load (mg cm^{-2})	-	-	-	~2.15	~2.04	~1.88	~1.78

To better guide the experiment, the impact of parameter variations on temperature during CTS experiments was summarized based on Fig. S6, 9. In pulse discharge mode, the voltage generally remains constant, while adjusting the current and time affects the temperature variation. Additionally, resistance fluctuations are typically controlled to be minimal to reduce error, in this experiment, the resistance was controlled at approximately 2.0 Ω. More parameters are shown in Table S3.

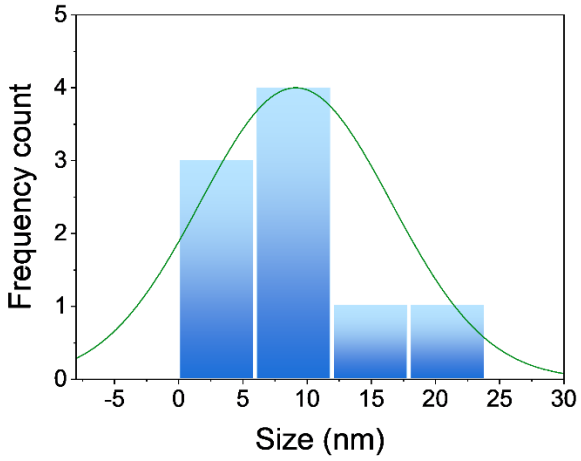

Fig. S10 Nanowire size statistics corresponding to Fig. 5g.

Table S4. The mass ratio of Si and O elements.

Samples	Elements (wt%)	
	Si	O
a-SiNWs@CC	3.5	1.0
c-SiNWs@CC	3.2	1.0
a-SiNWs@CC (Yellow volatiles)	2.5	1.0

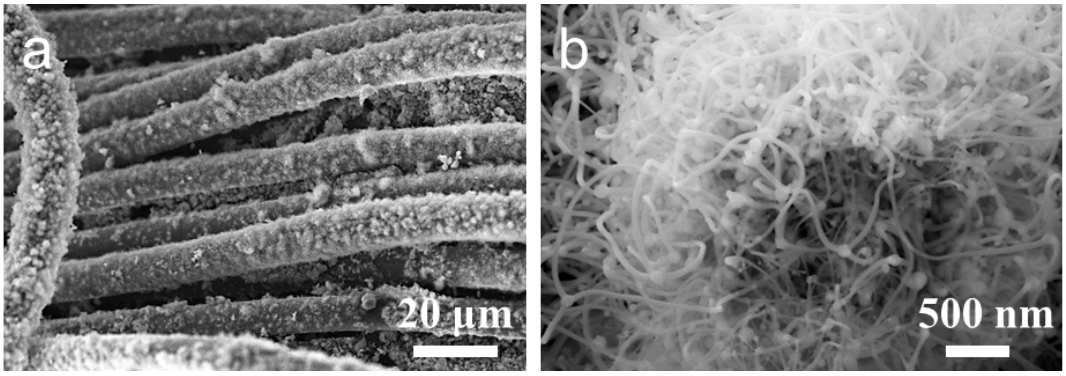

Fig. S11 (a, b) SEM morphology of c-SiNWs@CC without added copper salt.

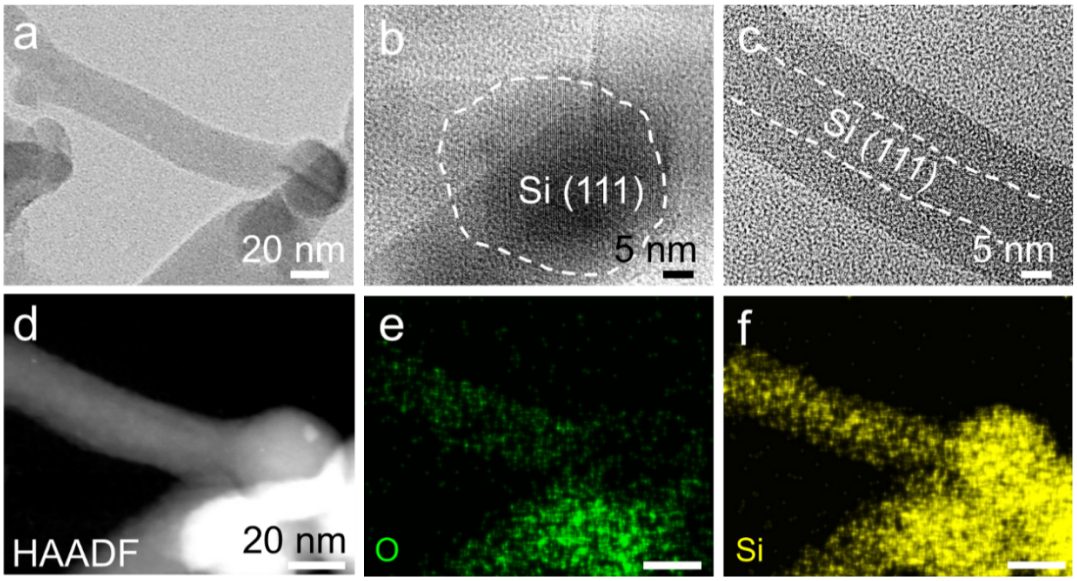

Fig. S12 (a) TEM, (b, c) HRTEM, (d-f) HAADF, and the corresponding O and Si element mapping images of c-SiNWs@CC material.

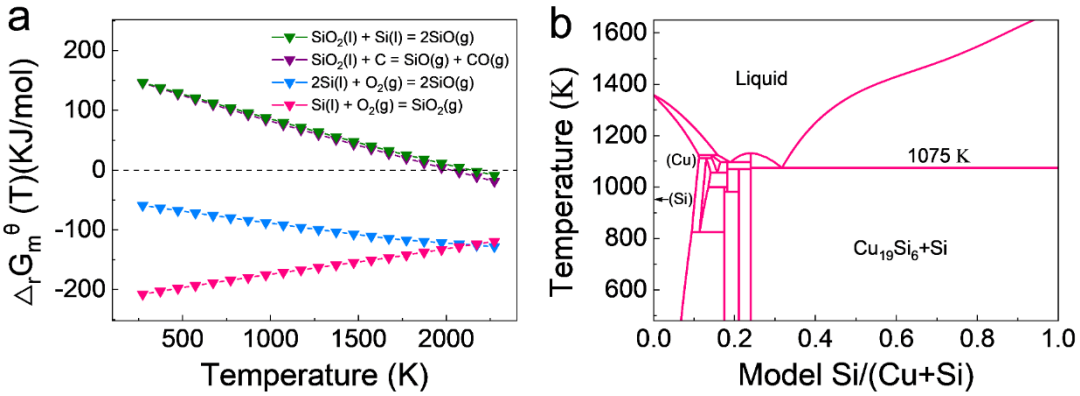

Fig. S13 (a) Standard Gibbs free energy charge ($\Delta_r G_m^{\theta}$) of gaseous SiO formation reaction; (b) Cu-Si binary alloy phase diagram. In the ~2000 K system, gaseous SiO may be generated as follows: $SiO_2(l) + Si(l) = 2SiO(g)$; $SiO_2(l) + C = SiO(g) + CO(g)$; $2Si(l) + O_2(g) = 2SiO(g)$. SiO_2 in the system comes from the oxide film on the surface of WSi powder and Si reacts with oxygen in the system at high temperature.[4]

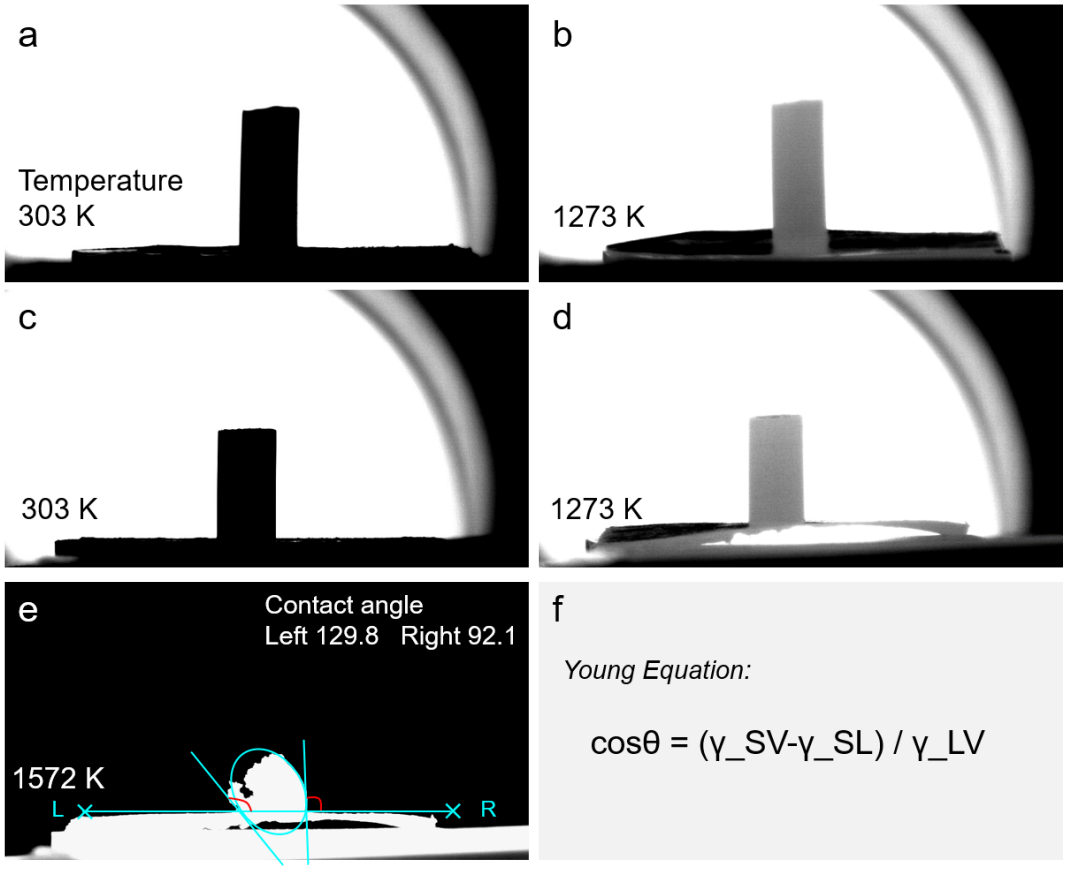

Fig. S14 (a, b) wSi, (c, d) wSi and Cu powder mixture (with a Cu mass fraction of 5 wt%) in the molten state at high temperatures of 303 K and 1273 K; (e, f) Contact angle measurement process and Young Equation, where θ is the contact angle, γ_SV represents the surface tension between a solid and a gas, γ_SL represents the surface tension between a solid and a liquid, and γ_LV represents the surface tension between a liquid and a gas.

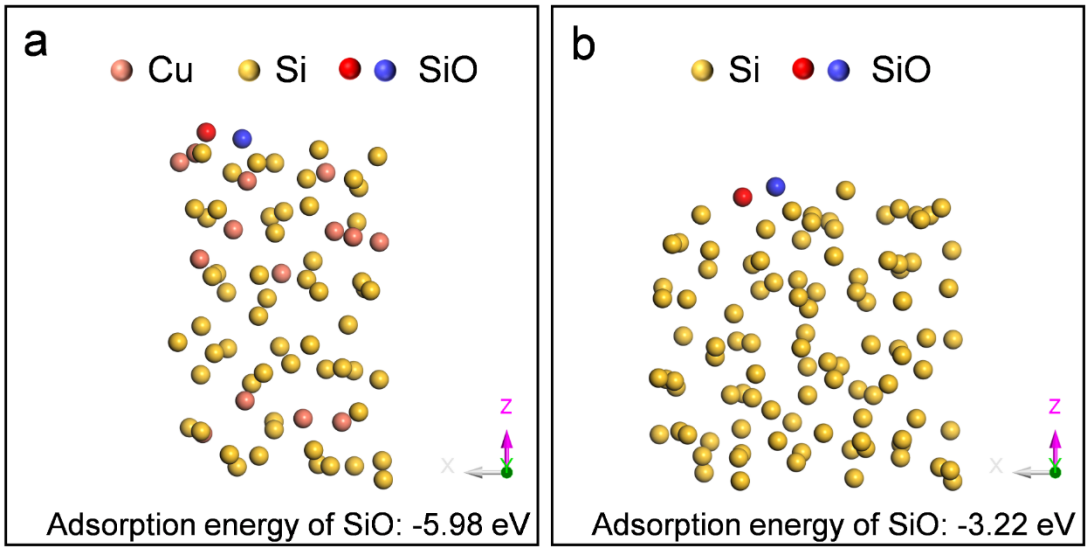

Fig. S15 Adsorption energy of SiO: (a) with Cu and (b) without Cu.

Computation details

Our first-principles calculations were carried out within DFT as implemented in the Vienna Ab Initio Simulation Package (VASP). The generalized gradient approximation (GGA) with the Perdew-Burke-Ernzerhof (PBE) function was employed to describe the electron exchange and correlation energies. The projected augmented wave (PAW) pseudopotentials were utilized to consider electron-ion interactions. The cutoff energy was set to be 500 eV for the plane-wave expansion. The criterion for geometry optimization in all calculations was set (10^{-5} eV), forces (2 x 10^{-2} eV $Å^{-1}$), and 0.05 eV for smearing. The first Brillouin zone was sampled by 4 x 4 x 1 and 3 x 4 x 1 Gamma k-point meshes for liquid Si and Si-Cu melt, respectively. The VASPKIT code was employed to finish the pre-processing of structural data. The analysis and visualization of atomic configurations relied on the VESTA package.

Si-O adsorption energy calculation

The appropriate numbers of Si atoms and Cu atoms based their densities were placed in a box to simulate liquid Si and Si-Cu melt. The Si-O atmosphere was represented by an atomic pair consisting of a Si atom and an O atom. The optimized Si-O atomic pair

and liquid Si and Si-Cu melt were placed in a box for the state of Si-O absorption. To weaken the artificial periodic interactions, vacuum layers along z-axis with a thickness about 15 Å were added. Several configurations were calculated simultaneously to determine the optimal adsorption site for minimize the adsorption energy. The Si-O adsorption energy was defined as follows:

$E_{ad} = E_{total} - E_{Si-O} - E_{sub}$

Where E_{total}, E_{Si-O}, E_{sub} represented the energy of the total configurations, Si-O atomic pair and the adsorption substrate (liquid Si and Si-Cu melt), respectively.

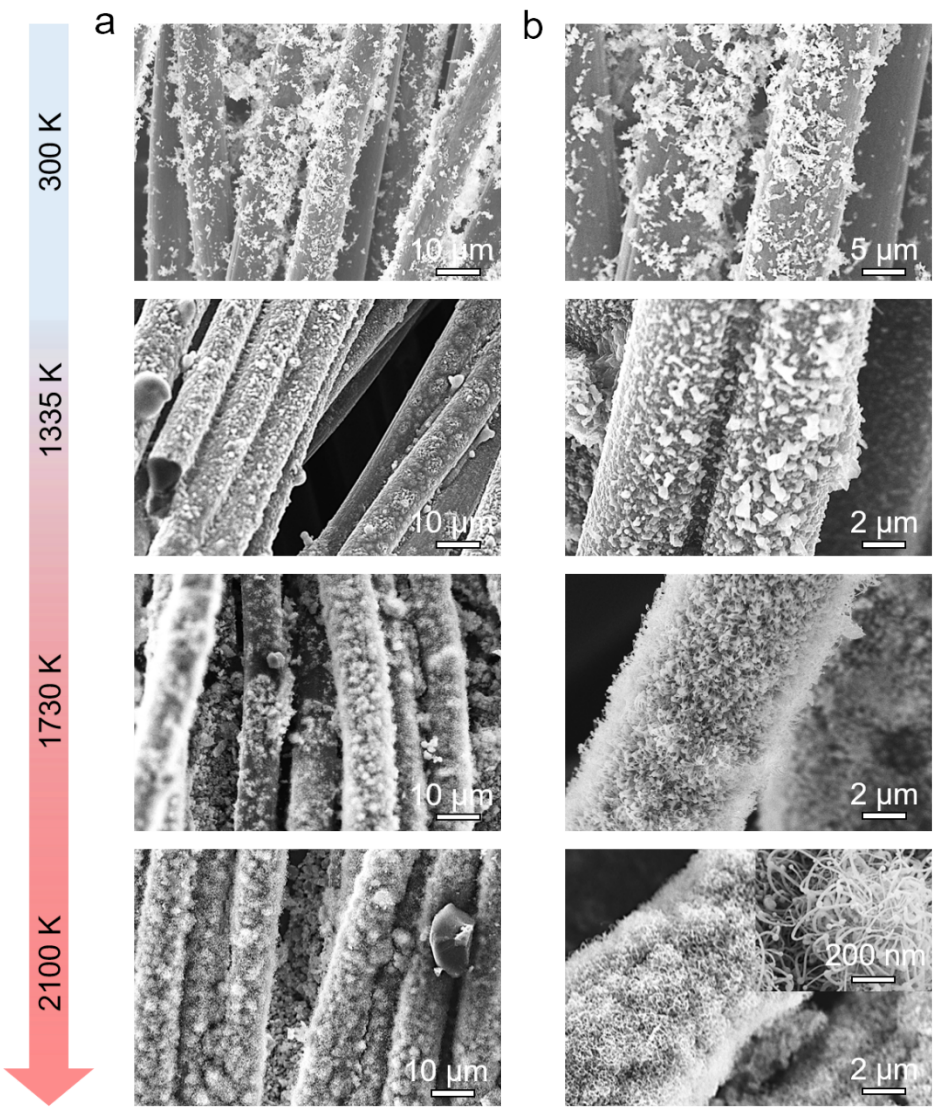

Fig. S16 (a, b) SEM of reactions at different temperatures of a-SiNWs@CC.

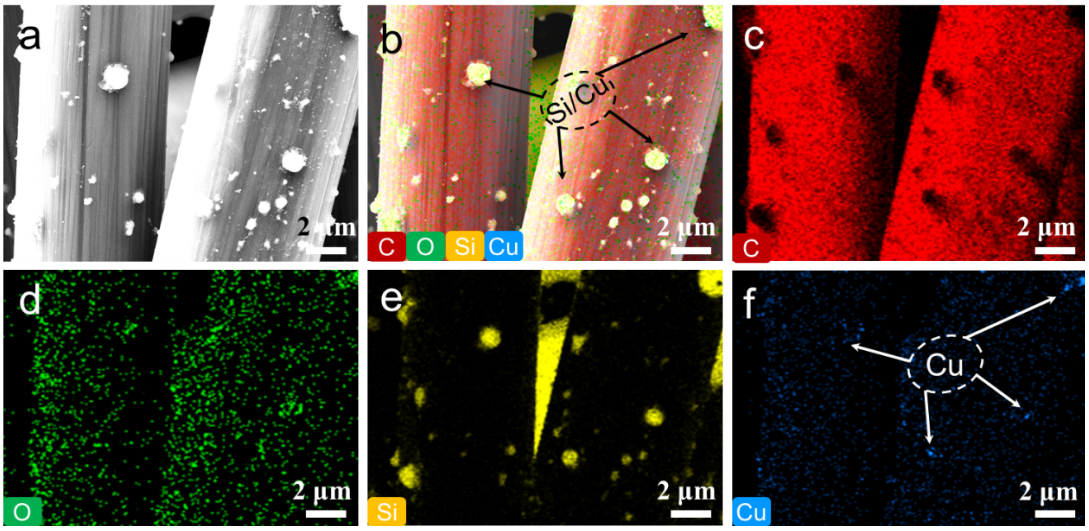

Fig. S17 Scattered tiny particles appearing on a-SiNWs@CC material during the CTS process. (a) SEM of the fine particles captured at the edges of the carbon cloth substrate after reaction; (b) EDS element mapping overlay and (c-f) distribution of C, O, Si, Cu elements, respectively. This suggests that during the CTS process, the Cu from the thermal decomposition of Cu sulfate and the Si from the WSi underwent fusion to form a eutectic mixture. This provides important support for elucidating the intermediate process of Si nanowires growth.

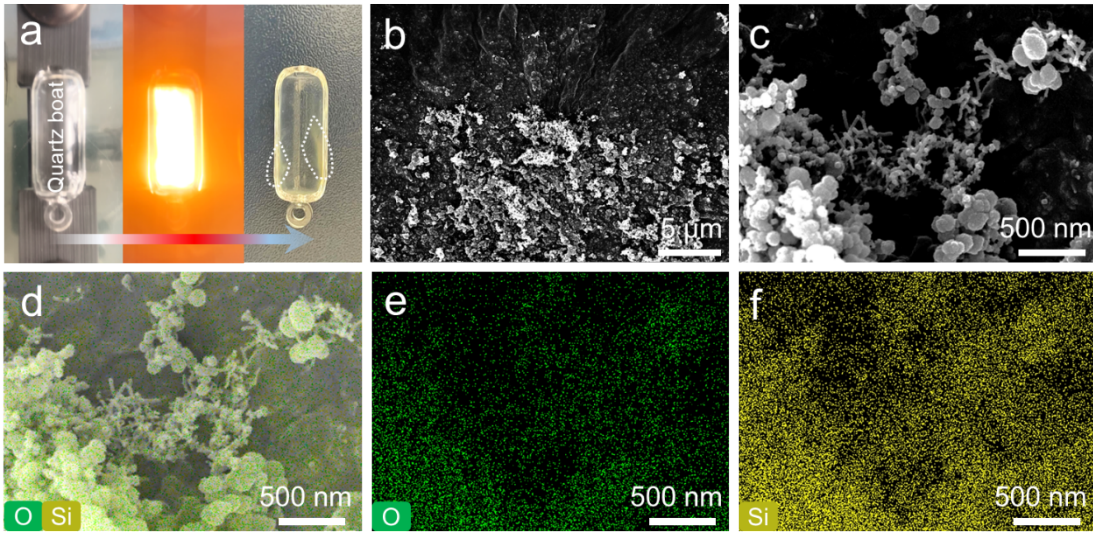

Fig. S18 (a) Investigation of volatile components captured during the CTS process; (b-f) SEM and EDS element mapping of yellow volatiles in the quartz boat. These particulate materials mainly consist of Si and O, with an elemental mass ratio of approximately 2.5:1. Also, scattered nanowires were observed (Fig. S18c), which may result from the condensation and deposition of some SiO_x vapors generated at high temperatures.[4, 5]

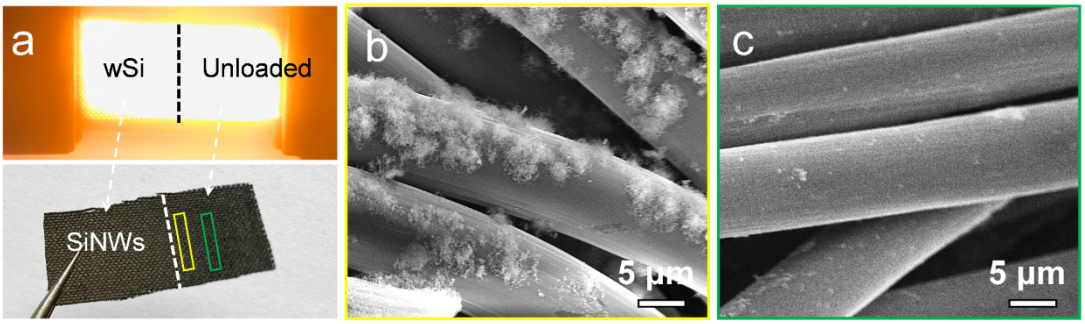

Fig. S19 (a) Optical image of the carbon cloth with half of the area loaded with wSi. Corresponding regions in the yellow box (b) and green box (c).

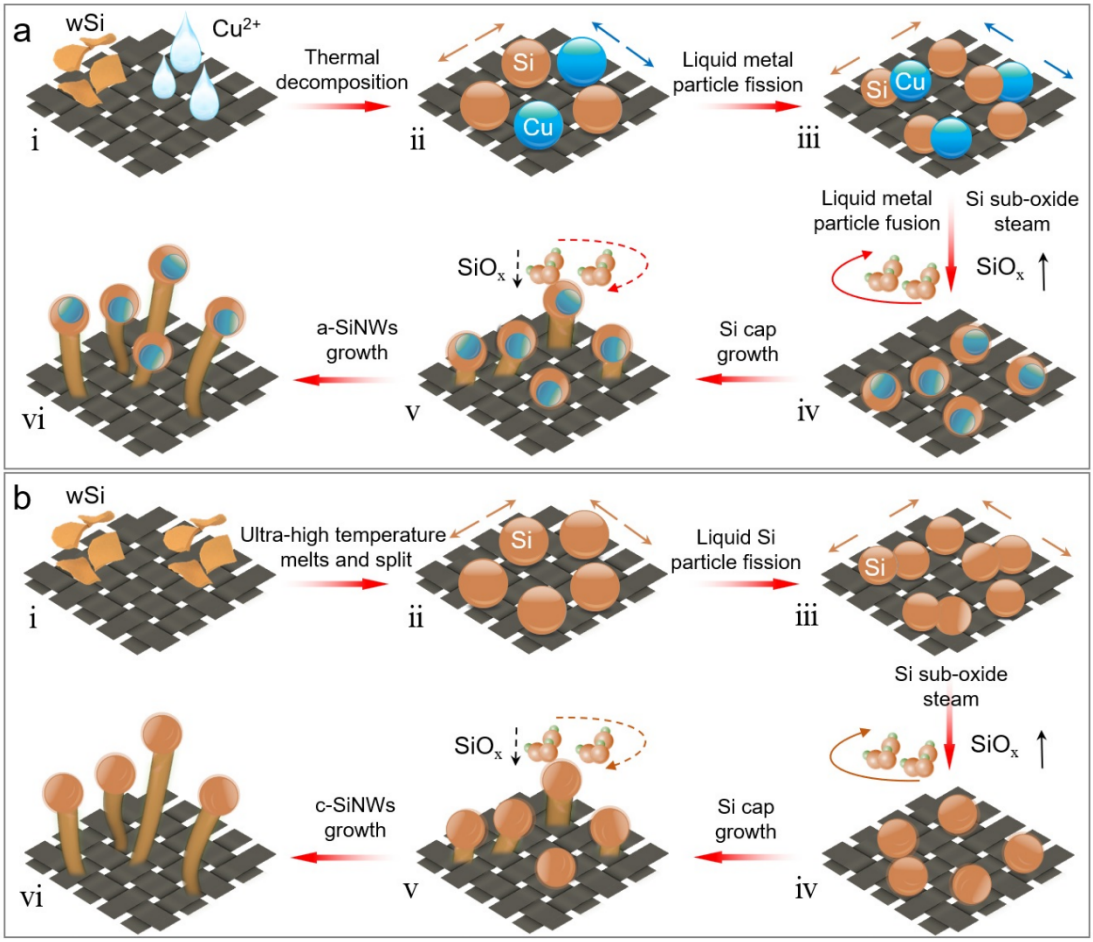

Fig. S20 Schematic diagrams of the (a) a-SiNWs@CC and (b) c-SiNWs@CC formation mechanism. The c-SiNWs@CC growth process goes through the following main stages: (i) Initial wSi physically contacts and adheres to the carbon cloth. (ii) Upon the onset of high-temperature CTS, wSi melts, and split to form particles. (iii) The formed particles further fission and become smaller on the carbon cloth. (iv) This is accompanied by the volatilization of Si sub-oxides steam (SiO_x). (v) The Si core with a SiO_x shell continuously adsorbs free Si atoms in the thermal field, acting as nuclei for Si nanowires growth. (vi) Directed diffusion driven by a high-gradient thermal field leads to the formation of crystalline Si nanowires. In addition, the Si nanowires tip was in the molten state during the growth process, which is conducive to adsorption and diffusion of atoms. This is also the main reason for formation of the thick crystalline Si nanowires tips. The outer layer of the nanowire is composed of SiO_x generated by decomposition of SiO, which can restrict the nanowire growth in a non-one-dimensional direction.[6-8]

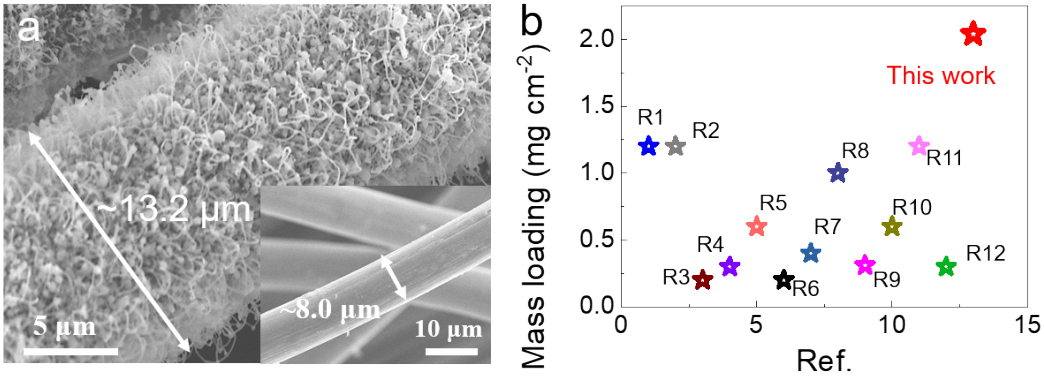

Fig. S21 (a) Diameter change in carbon cloth before and after loading with Si nanowires; (b) Comparison of surface loading of Si nanowires in this work with those electrodes previously reported (Table S5).

Table S5 Comparison of the mass loading of some Si-based anodes.

Materials and structures	Mass loading (mg cm^{-2})	Current density (A g^{-1})	Cycles	Reversible capacity (mAh g^{-1})	Ref.
a-SiNWs@CC	**2.04**	**0.8**	**200**	**2900**	**This work**
Cu/Si/Ge NW array	1.2	0.4	100	1052	R1 [9]
3D Cu_xSi_y NF	1.2	0.25	550	1655	R2 [10]
$Cu_{15}Si_4$ NWs array	0.2	0.8	200	2000	R3 [11]
$Si_{1-x}Ge_x$ NWs array	0.3	0.8	250	1360	R4 [12]
SiNW-Gr array	0.6	0.4	200	2400	R5 [13]
Si NWs array	0.2	0.8	250	1605	R6 [14]
Ge@aSi NWs array	0.4	0.8	150	1455	R7 [15]
Si-Ge/Si core shell NW	1.0	0.24	400	1031	R8 [16]
Ge/Si core shell NW	0.31	0.24	100	1614	R9 [17]
C-SiO_x@Si/rGO	0.4-0.8	1.0	100	925.4	R10 [18]
Si@SiO_x@C	1.2	1.0	300	1600	R11 [19]
Si + rGO@DFAT-C	0.3	0.5	200	968	R12 [20]

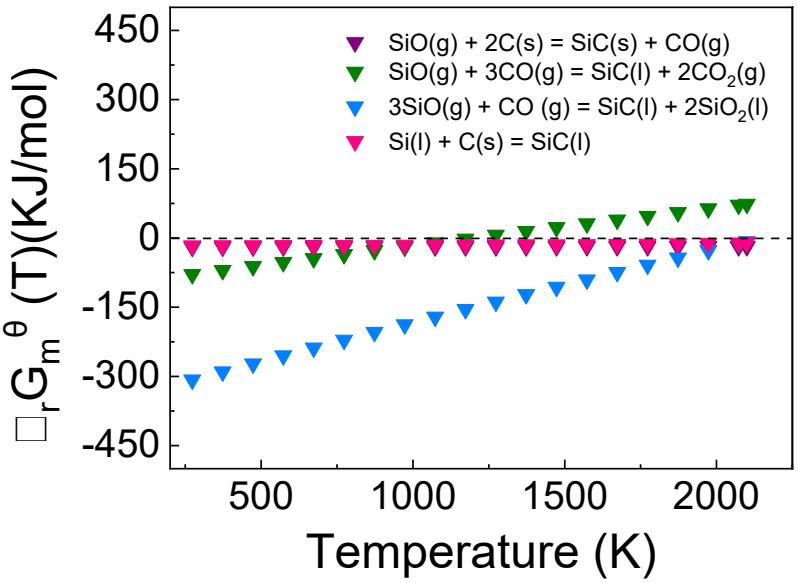

Fig. S22 The standard Gibbs free energy charge ($\Delta_rG_m^{\theta}$) of the reaction that may produce SiC by the CTS. During the synthesis of Si nanowires, the carbon source provided by carbon cloth will react with active Si (Si and SiO) to form SiC at high temperatures. The following reaction occurs: SiO(g) + 2C(s) = SiC(s) + CO(g); SiO(g) + 3CO(g) = SiC(l) + $2CO_2$(g); 3SiO(g) + CO(g) = SiC(l) + $2SiO_2$(l); Si(l) + C(s) = SiC(l).

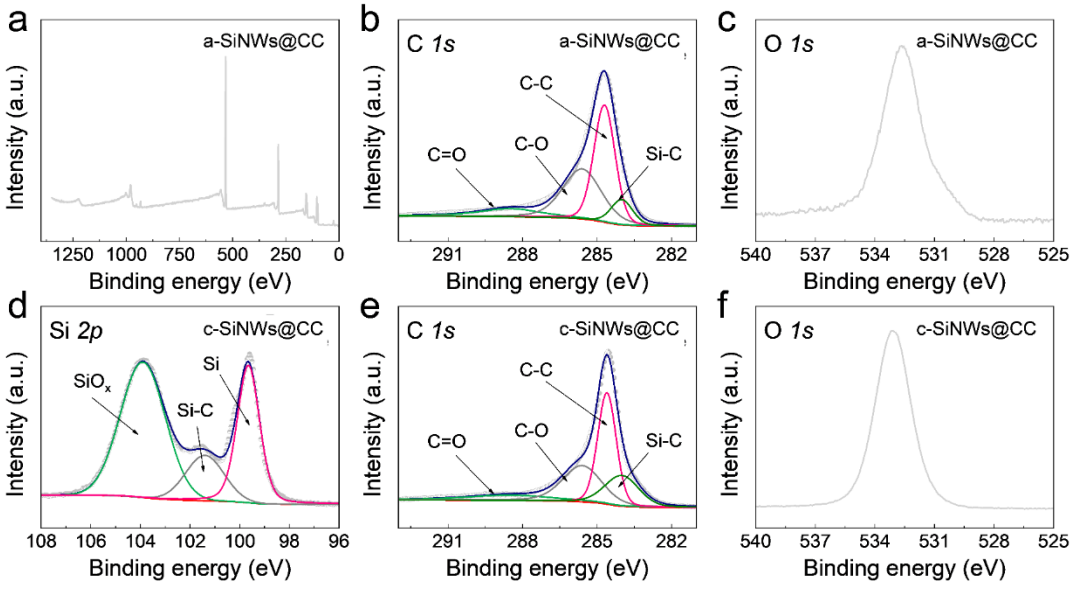

Fig. S23 XPS Si 2p, C 1S, O 1s spectra of (a-c) a-SiNWs@CC and (d-f) c-SiNWs@CC materials.

Table S6. Comparison of Si nanowire electrodes reported in recent years.

Electrodes	Current (1C= 3579 mA g^{-1})	ICE (%)	Cycle number	Capacity (mAh g^{-1})	Retention rate (%)	Ref.
a-SiNWs@CC	**0.8 A g^{-1}**	**91.35**	**200**	**2900**	**95**	**Our work**
Si NWs@3D-CS	C/10	62	900	1782	88	R1 [21]
Si NWs@SS	C/10	81	140	2437.5	75	R2 [22]
Cu_3Si/Si nanowires	0.2 A g^{-1}	88.94	100	1656	63	R3 [23]
Si NWs@C	0.5 A g^{-1}	76.36	200	781	80	R4 [24]
Si NW@NbHQ-500	0.2 A g^{-1}	71.6	120	1280	40	R5 [25]
SnS−SiGt	C/20	77	200	822	60	R6 [26]
SiPA/CNT	0.2 A g^{-1}	54.7	200	1925	70	R7 [27]
SiO/Si/C NWs	0.05 C	53.4	100	1763	72	R8 [28]
C/Si NW/GM	0.2 C	76.2	50	587	66	R9 [29]
PH-Si NWs	0.2 A g^{-1}	57	1000	1602	54	R10 [30]
Si-NWs	0.05 C	84	100	2926	78	R11 [31]
Gt−Si NW	C/20	72	300	751	43	R12 [32]
SiO_x/S NWs@C	0.05 C	74.6	200	1336	80	R13 [33]
Ge@aSi NWs	C/10	80	150	1330	90	R14 [34]
p/w-mSi	0.2 A g^{-1}	80	100	1830.5	75.3	R15 [35]
Si NW	0.2 C	82	200	1640	76	R16 [36]

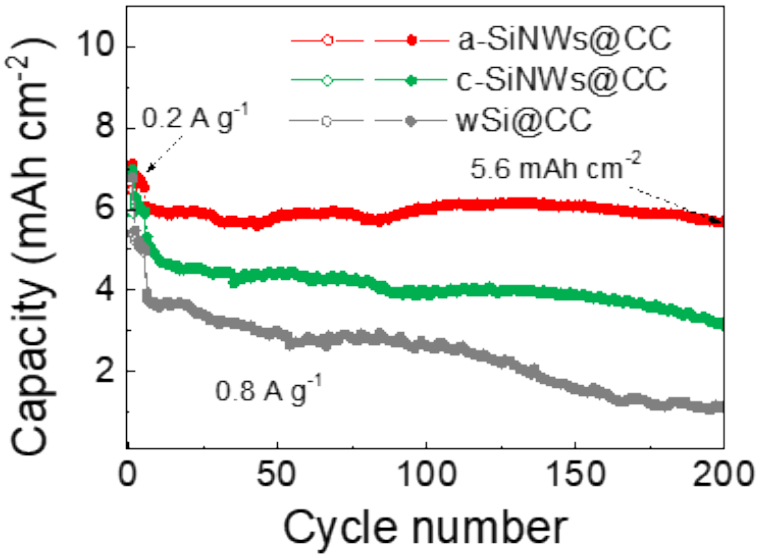

Fig.S24 Areal capacity corresponding to the conversion in Fig. 5c.

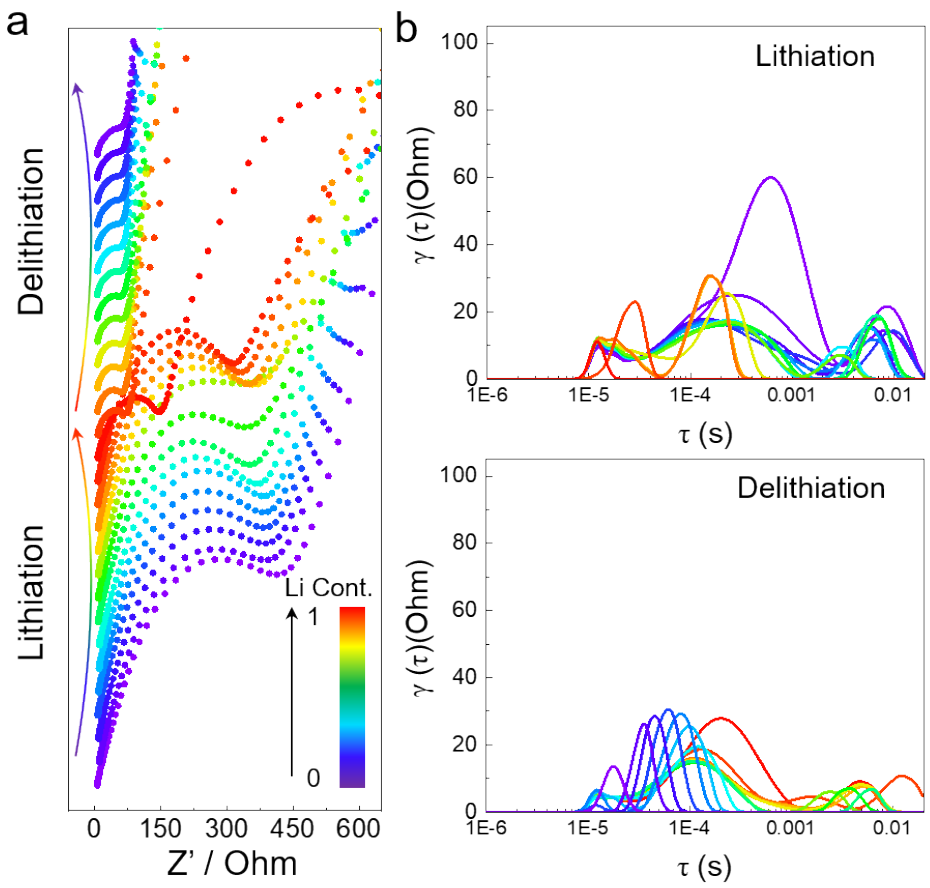

Fig. S25 In-situ EIS impedance plots and corresponding DRT curves for wSi@CC electrodes during the first (de)lithiation.

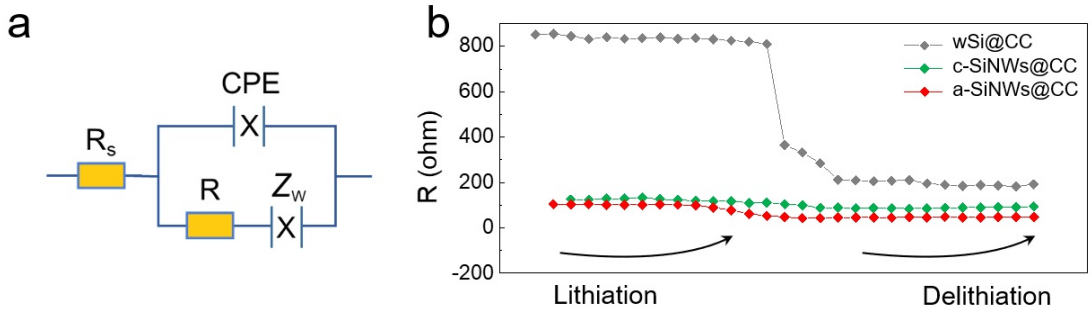

Fig. S26 (a) Equivalent circuit diagram; (b) Fitted values of R. Generally, as shown in the Figs. S25 and 5a, c, the overall shape of EIS plots have the common feature with high-/middle- frequency depressed semicircles followed by a sloped line in the lower-frequency range. The Fig. S26a shows the fitted equivalent circuit, where the symbols of R_S, R, indicate the solution resistance, the diffusion resistance of Li ions through SEI layer and the charge-transfer resistance, respectively.[37]

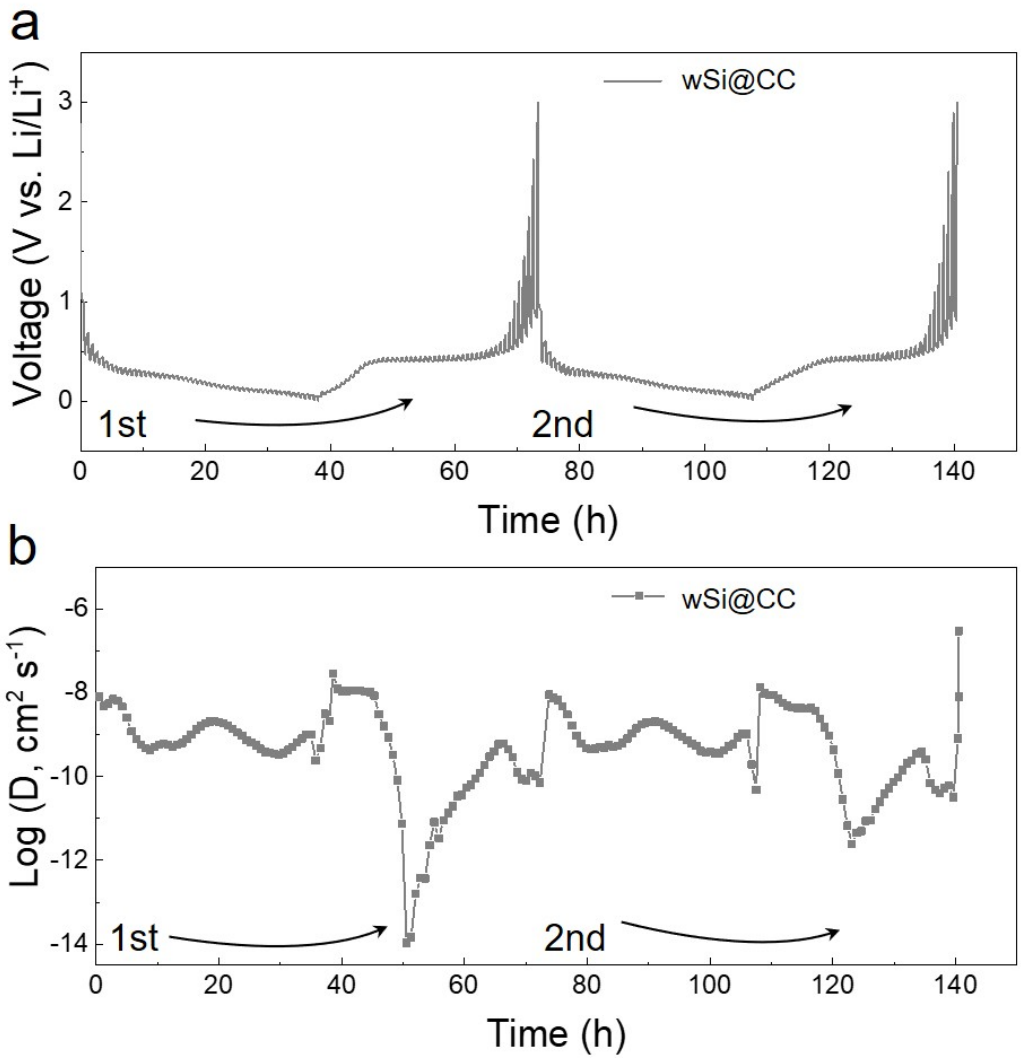

Fig. S27 GITT test curves of wSi@CC. In general, according to the following Fick's Second law (simplified formula):[20, 38]

$$D_{Li+} = \frac{4L^2}{\pi\tau}\left(\frac{\Delta E_S}{\Delta E_\tau}\right)^2$$

where L (cm) is the diffusion length of lithium ion (for the dense electrode, L (cm) is the electrode thickness); τ is constant current time, ΔES and $\Delta E\tau$ are voltage change and total voltage change.

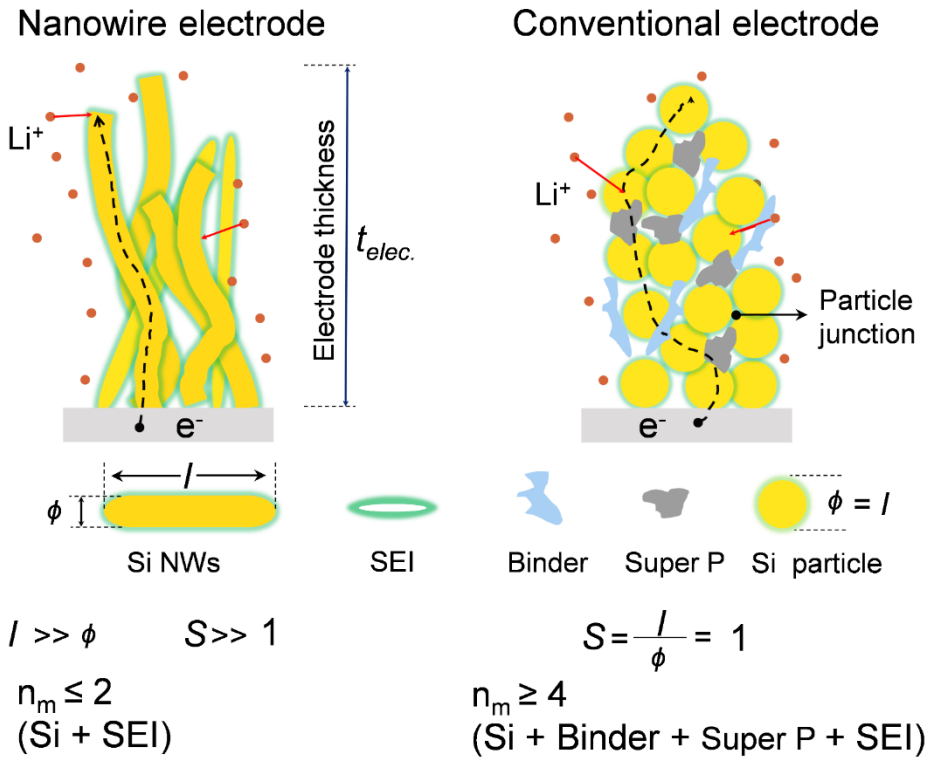

$$n_{junc.} \approx \frac{t_{elec.}}{S} - 1 \quad \text{(Number of particle junction)}$$

$$R_C \propto n_m \times n_{junc.}$$

$$\text{Conductivity: } \sigma_{electrode} \approx \frac{1}{(R_C A/L) + 1/\sigma_0}$$

σ_0 : Intrinsic conductivity

R_C: Interparticle contact resistance

A certain electrode thickness:

$$\sigma_{Nanowire} >> \sigma_{Conventional}$$

Fig. S28 Comparison of electron transport advantages between nanowire electrode and conventional electrode. Tightly entangled Si NWs with a long aspect ratio (*S*) not only reduce the number of inter-particle junctions ($n_{junc.}$) through which a charge carrier (e.g., electron) needs to travel along the electrode thickness but also alleviate the impact of SEI formation on electrode polarization. Electrode conductivity expression including contact resistance and its correlation with particle aspect ratio and number of existing media (n_m, different electrode components) predicts higher conductivity for an electrode comprised of Si NWs than that of a conventional electrode with a comparable electrode thickness ($t_{elec.}$) and particle diameter (Φ).[36]

The calculation detail for simulation model:

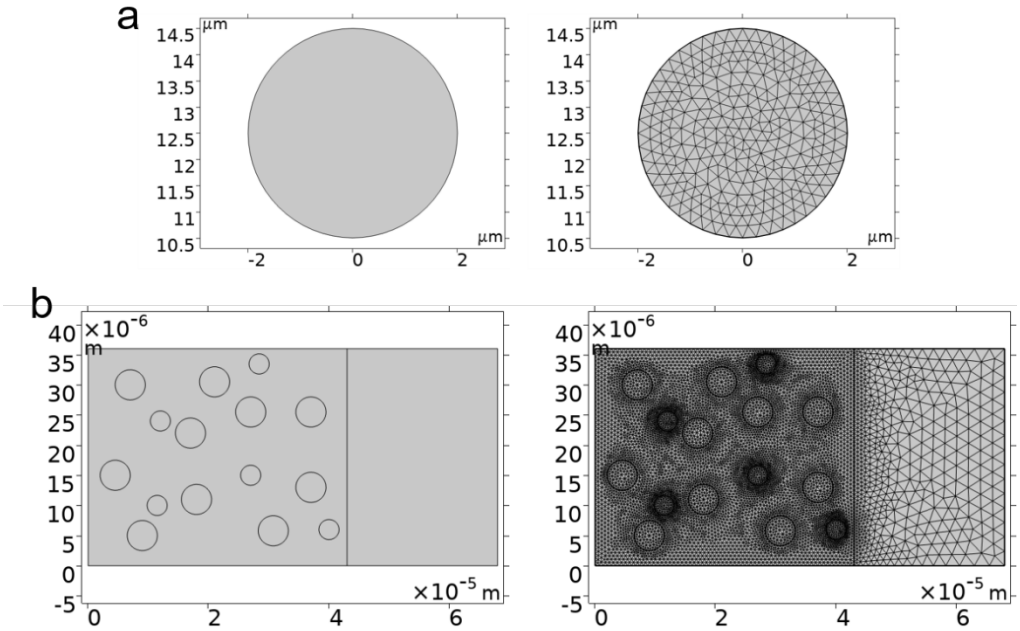

Fig. S29 Two-dimensional geometry. (a) Single particle, and (b) multiple Si particles randomly distributed on the carbon substrate. The two-dimensional model structure is depicted in Fig. S29, illustrating the lithiation stress changes of single a-Si and c-Si particles, as well as the electrode stress variations of Si particles on the carbon-based substrate. Coupled calculations are conducted using the lithium-ion battery - solid mechanics - dilute species transport model. As shown in Fig. S29b, the electrode region comprises the carbon substrate, randomly distributed Si particles (circular), a separator, and the lithium metal surface boundary. The fundamental computational process is outlined as follows:

First, the charge and discharge process of Si is calculated based on a classical battery model to obtain the lithium concentration distribution within the active particles:

$$C_{Li} = C_{Li,s} - \left(\frac{R_{Li}}{k_{eff}}\right)\cdot\Delta t$$

where C_{Li} is the current lithium concentration, $C_{Li,s}$is the surface lithium concentration, R_{Li} is the lithium reaction rate, and k_{eff} is the effective reaction rate constant.

Then, based on the relationship between the volume expansion of the Si particles and the state of charge (*SOC*) curve, the force exerted on the carbon substrate due to the

volume change of the lithiated particles at a given moment is calculated. This force induces strain in the carbon-based substrate, enabling the determination of the force distribution within the electrode.

$$\Delta V = V_0 \cdot \beta \cdot SOC$$

$$F = \Delta V \cdot \frac{dP}{dV}$$

where ΔV is volume change, V_0 is the initial volume, β is the volume expansion coefficient, *SOC* is the state of charge ratio, F is the applied force, and $\frac{dP}{dV}$ is the pressure change caused by the volume change.

In addition, the mass transport of Li in simulated anode was controlled by Fick's second law:

$$\frac{\partial c_{Li}}{\partial t} + \nabla \cdot (-D \nabla c_{Li}) = 0$$

where D is the diffusivity of Li was set as a nonlinear function of Li concentration to simulate the chemical reaction and diffusion in a unified manner:

$$D = D_0 \exp\left(-\frac{E_a + P \cdot \sigma}{RT}\right)$$

where D_0 is the diffusion coefficient at zero stress, *Ea* is the activation energy for diffusion, P is the stress sensitivity coefficient, σ is the stress, R is the gas constant, and T is the temperature.

The total strain is the sum of elastic strain and chemical strain:

$$\epsilon_{ij} = \epsilon_{ij}^{c} + \epsilon_{ij}^{c}$$

$$\sigma_{ij} = C_{ijkl} \epsilon_{kl}$$

$$\epsilon_{ij}^{c} = \beta_{ij} \cdot (C_{Li} - C_{Li0})$$

where σ_{ij} is the stress tensor, C_{ijkl} is the elastic tensor, and ϵ_{kl} is the strain tensor, β_{ij} is the expansion coefficient and C_{Li0} is the reference lithium concentration without strain. The calculation of expansion considers the boundary conditions: in the geometric model, the lithium metal surface and the upper and lower boundaries are set as fixed conditions, while the left side of the electrode region is defined as a free boundary.

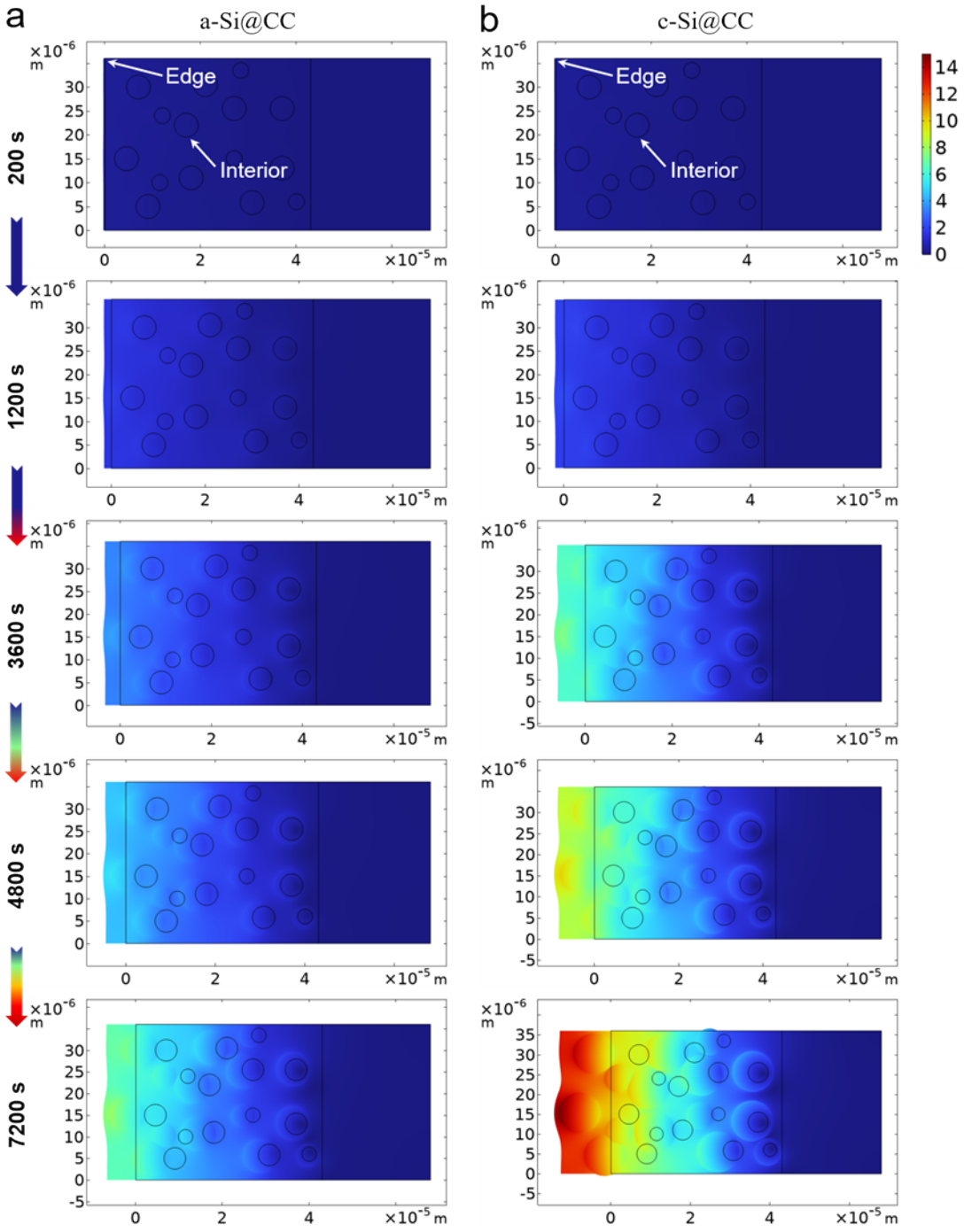

Fig. S30 The electrode displacement during (a) a-Si and (b) c-Si lithiation at different time intervals (200 s, 1200 s, 3600 s,4800s, and 7200s).

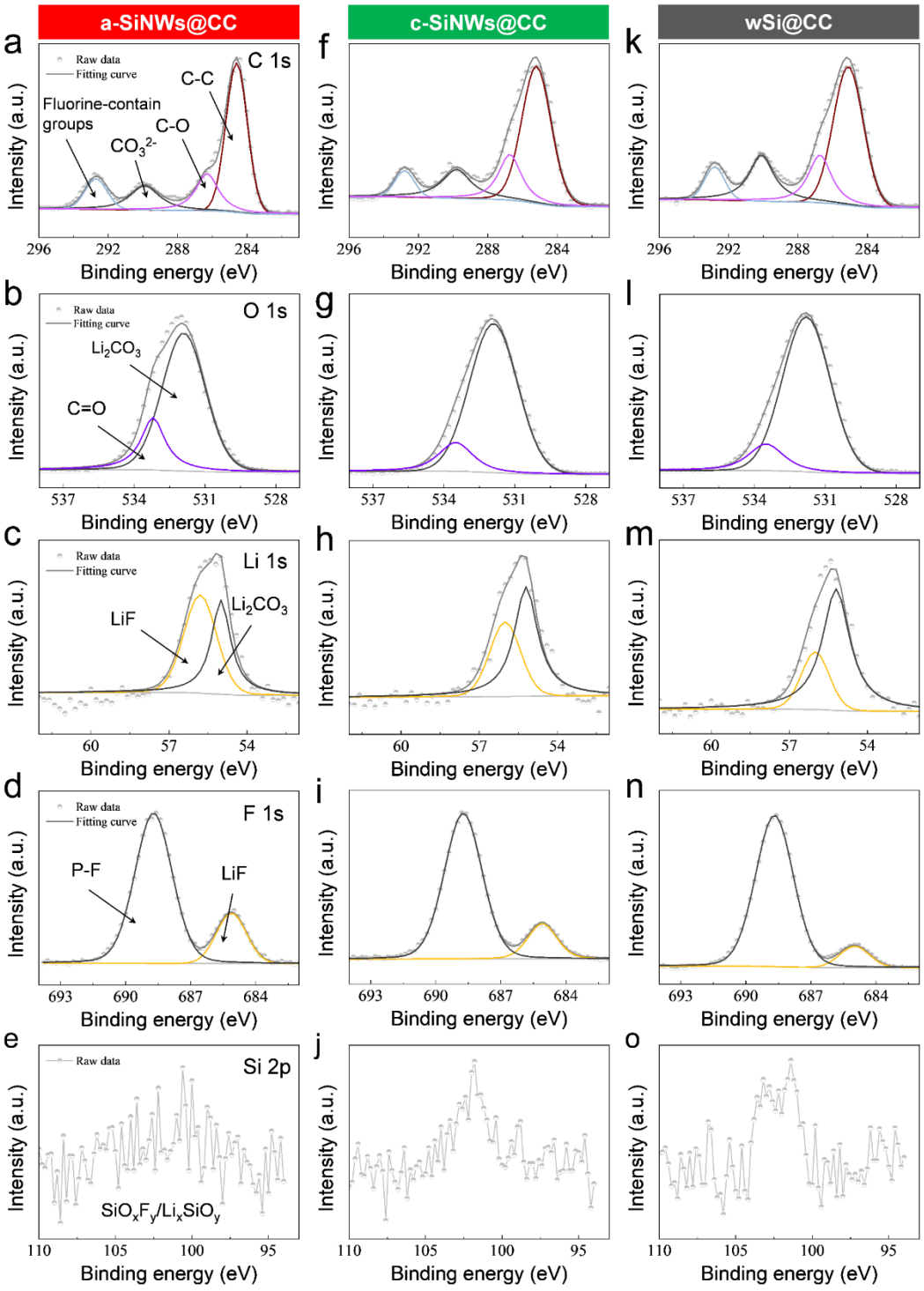

Fig. S31 C 1s, O 1s, Li 1s, F 1s, and Si 2p XPS spectra of the (a-e) a-SiNWs@CC, (f-j) c-SiNWs@CC, and wSi@CC electrodes after 100 cycles.

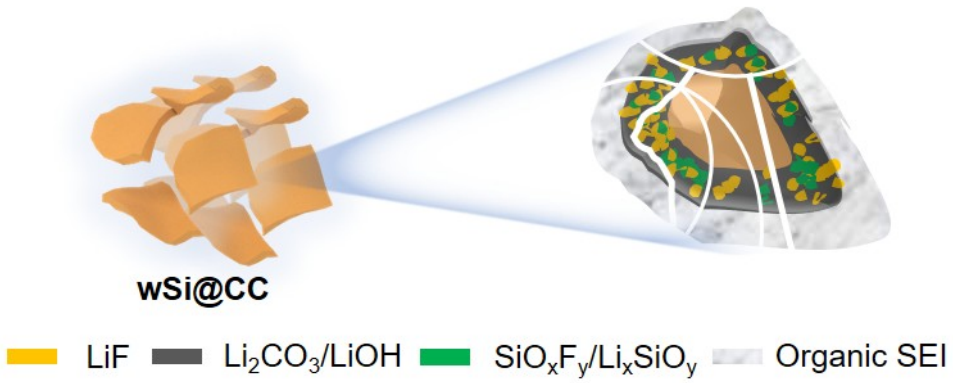

Fig. S32 Schematic comparison of SEI on the surface of wSi@CC after cycling.

References

[1] H. Wang, H. Wang, S. Zhang, Y. Zhang, K. Xia, Z. Yin, M. Zhang, X. Liang, H. Lu, S. Li, J. Zhang, Y. Zhang, *Nano Research* **2021,** *15*, 2576.

[2] J.-Y. Song, C. Kim, M. Kim, K. M. Cho, I. Gereige, W.-B. Jung, H. Jeong, H.-T. Jung, *Science Advances* **2021,** *7*, 1.

[3] X. Li, F. Chen, B. Zhao, S. Zhang, X. Zheng, Y. Wang, X. Jin, C. Dai, J. Wang, J. Xie, Z. Zhang, Y. Zhao, *Nanomicro Lett* **2023,** *15*, 1.

[4] J. Lu, J. Liu, X. Gong, S. Pang, C. Zhou, H. Li, G. Qian, Z. Wang, *Energy Storage Materials* **2022,** *46*, 594.

[5] S. Xu, X. Hou, D. Wang, L. Zuin, J. Zhou, Y. Hou, M. Mann, *Advanced Energy Materials* **2022,** *12*, 2200127.

[6] Y. Yao, S. Fan, *materials letters* **2006,** *61*, 177.

[7] V. Schmidt, J. V. Wittemann, U. Gosele, *Chemical Reviews* **2010,** *110*, 361.

[8] V. Schmidt, J. V. Wittemann, S. Senz, U. Gosele, *Adv Mater* **2009,** *21*, 2681.

[9] Q. Zhang, H. Chen, L. Luo, B. Zhao, H. Luo, X. Han, J. Wang, C. Wang, Y. Yang, T. Zhu, *Energy Environmental Science* **2018,** *11*, 669.

[10] I. S. Aminu, H. Geaney, S. Imtiaz, T. E. Adegoke, N. Kapuria, G. A. Collins, K. M. Ryan, *Advanced Functional Materials* **2020,** *30*, 2003278.

[11] K. Stokes, H. Geaney, M. Sheehan, D. Borsa, K. M. Ryan, *Nano letters* **2019,** *19*, 8829.

[12] K. Stokes, H. Geaney, G. Flynn, M. Sheehan, T. Kennedy, K. M. Ryan, *ACS nano* **2017,** *11*, 10088.

[13] F. Xia, S. Kwon, W. W. Lee, Z. Liu, S. Kim, T. Song, K. J. Choi, U. Paik, W. I. Park, *Nano letters* **2015,** *15*, 6658.

[14] K. Stokes, T. Kennedy, G.-T. Kim, H. Geaney, D. Storan, F. Laffir, G. B. Appetecchi, S. Passerini, K. M. Ryan, *Nano Letters* **2020,** *20*, 7011.

[15] K. Stokes, W. Boonen, H. Geaney, T. Kennedy, D. Borsa, K. M. Ryan, *ACS applied materials interfaces* **2019,** *11*, 19372.

[16] H. Kim, Y. Son, C. Park, M.-J. Lee, M. Hong, J. Kim, M. Lee, J. Cho, H. C. Choi, *Nano letters* **2015,** *15*, 4135.

[17] T. Kennedy, M. Bezuidenhout, K. Palaniappan, K. Stokes, M. Brandon, K. M. Ryan, *ACS nano* **2015,** *9*, 7456.

[18] T. Meng, B. Li, Q. Wang, J. Hao, B. Huang, F. L. Gu, H. Xu, P. Liu, Y. Tong, *ACS nano* **2020,** *14*, 7066.

[19] R. F. H. Hernandha, P. C. Rath, B. Umesh, J. Patra, C. Y. Huang, W. W. Wu, Q. F. Dong, J. Li, J. K. Chang, *Advanced Functional Materials* **2021,** *31*, 2104135.

[20] Q. Wang, T. Meng, Y. Li, J. Yang, B. Huang, S. Ou, C. Meng, S. Zhang, Y. Tong, *Energy Storage Materials* **2021,** *39*, 354.

[21] I. Saana Amiinu, S. Imtiaz, H. Geaney, T. Kennedy, N. Kapuria, S. Singh, K. M. Ryan, *Journal of Energy Chemistry* **2023,** *81*, 20.

[22] M. Rashad, H. Geaney, *Chemical Engineering Journal* **2023,** *452*, 139397.

[23] S. Jiang, J. Cheng, G. P. Nayaka, P. Dong, Y. Zhang, Y. Xing, X. Zhang, N. Du, Z. Zhou, *Journal of Alloys and Compounds* **2024,** *998*, 174996.

[24] Z. Fang, P. Zhou, Y. Tian, H. Fang, Q. Zhang, *Dalton Trans* **2024,** *53*, 9052.

[25] J. Fang, J. Li, W. Zhang, L. Qin, K. Wu, L. Hui, T. Gong, D. Li, Y. Hu, A. Li, H. Feng, *Chemical Engineering Journal* **2024,** *484*, 149387.

[26] C. Keller, S. Karuppiah, M. Raaen, J. Wang, P. Perrenot, D. Aldakov, P. Reiss, C. Haon, P. Chenevier, *ACS Applied Energy Materials* **2023,** *6*, 5249.

[27] Z. Hong, Z. Fang, Y. Luo, H. Wu, H. Tian, F. Zhao, Q. Li, S. Fan, J. Wang, *Journal of Materials Chemistry A* **2022,** *10*, 23509.

[28] Z. Yang, Y. Du, Y. Yang, H. Jin, H. Shi, L. Bai, Y. Ouyang, F. Ding, G. Hou, F. Yuan, *Journal of Power Sources* **2021,** *497*, 229906.

[29] B. Liu, P. Huang, Z. Xie, Q. Huang, *Energy & Fuels* **2021,** *35*, 2758.

[30] C.-B. Chang, C.-Y. Tsai, K.-T. Chen, H.-Y. Tuan, *ACS Applied Energy Materials* **2021,** *4*, 3160.

[31] J. H. Choi, H. K. Kim, E. M. Jin, M. W. Seo, J. S. Cho, R. V. Kumar, S. M. Jeong, *J Hazard Mater* **2020,** *399*, 122949.

[32] S. Karuppiah, C. Keller, P. Kumar, P. H. Jouneau, D. Aldakov, J. B. Ducros, G. Lapertot, P. Chenevier, C. Haon, *ACS Nano* **2020,** *14*, 12006.

[33] C. Shen, R. Fu, H. Guo, Y. Wu, C. Fan, Y. Xia, Z. Liu, *Journal of Alloys and Compounds* **2019,** *783*, 128.

[34] K. Stokes, W. Boonen, H. Geaney, T. Kennedy, D. Borsa, K. M. Ryan, *ACS Appl Mater Interfaces* **2019,** *11*, 19372.

[35] Q. Yu, Y. Liang, J. Liu, Y. Mu, H. Xu, X. Tang, S. Huang & X. Li, *ACS Applied Nano Materials*, **2022**, *5*, 17173-17182.

[36] A. Pendashteh, R. Tomey, J J.Vilatela, *Advanced Energy Materials* **2024**, 14, 2304018.

[37] L. Shen, P. Wang, C. Fang, Z. Lin, G. Zhao, S. Li, Y. Lin, Z. Huang, J. Li, *Small* **2024,** *20,* 2404135.

[38] X. Lin, J. Gao, K. Zhong, Y. Huang, H. Yao, Y. Lin, Y. Zheng, Z. Huang, J. Li, *Journal of Materials Chemistry A* **2022,** *10*, 23103.